ROYAL SOCIETY
OF CHEMISTRY

PAPER

Check for updates

Isovalent doping: a new strategy to suppress surface Sr segregation of the perovskite O_2-electrode for solid oxide fuel cells†

Bonjae Koo, [ID] ‡ Jongsu Seo, Jun Kyu Kim and WooChul Jung [ID] *

Surface Sr segregation and phase separation are the key reasons behind the chemical instability of Sr-containing perovskite oxide surfaces and the corresponding performance degradation of solid oxide fuel cell O_2-electrodes, but to date, practical solutions to prevent this phenomenon are limited. Here, we investigate how isovalent doping (in this case, Zr substitution of Ti) changes the surface morphology, chemical composition, and thus the O_2 activation kinetics under actual operating conditions. Thin films of $SrTi_{0.5}Fe_{0.5}O_{3-\delta}$ as a representative model perovskite O_2-electrode, with Zr doping, are fabricated *via* pulsed laser deposition and their surface oxygen exchange rates are then characterized *via* electrical conductivity relaxation assessments. Zr dopants strengthen the Sr–O bonds in the oxide lattice, inhibiting the formation of surface SrO_x clusters and significantly reducing the deterioration of the oxygen exchange rates compared to the results from undoped film at 650 °C for 30 h. These observations suggest a new strategy for ensuring the surface stability of Sr-containing perovskite oxides for fuel cell O_2-electrodes.

Introduction

Solid oxide fuel cells (SOFCs) are currently attracting much attention as a promising sustainable power generator.[1] The direct electrochemical conversion of electricity from the chemical energy of fuel increases the energy conversion efficiency, and high-temperature operation makes it possible to use a variety of fuels other than hydrogen.[2–11] A key step during typical SOFC energy-conversion processes is the oxygen reduction reaction (ORR) at O_2-electrodes, in which the rapid exchange of O_2 at the electrode surface is critical to facilitate the overall reaction rate. Sr-based perovskite oxides such as $(La,Sr)CoO_{3-\delta}$, $(La,Sr)(Co,Fe)O_{3-\delta}$, $(Ba,Sr)(Co,Fe)O_{3-\delta}$, $Sr(Ti,Fe)O_{3-\delta}$ and $Pr(Ba,Sr)(Co,Fe)_2O_{5+\delta}$ are widely used as SOFC O_2-electrode materials given their high electronic and ionic conductivity levels and favorable catalytic activity for electrode reactions.[11–19] However, a type of surface deterioration phenomenon, specifically Sr segregation, is known to be one of the crucial barriers preventing the realization of a rapid oxygen exchange rate in Sr-containing perovskite oxides. It has been reported that under high-temperature operating conditions, Sr selectively accumulates on the perovskite surface, leading to the formation of SrO_x-type dielectric precipitates, which severely degrade the oxygen reduction activity of $(La,Sr)CoO_{3-\delta}$, $(La,Sr)MnO_{3-\delta}$ or $Sr(Ti,Fe)O_{3-\delta}$ electrodes.[19–36]

Despite extensive research efforts to understand and prevent Sr segregation, progress has been unsatisfactory thus far.[19–44] This is partly due to the fact that a majority of relevant studies have been complicated by their use of typical ceramic pellets or powders with ill-defined surface chemical and structural features, whereas Sr segregation is fundamentally a surface reaction. Previously, we addressed this issue through the microfabrication of epitaxial or highly textured thin-film structures with well-defined surfaces and high purity levels.[6,23,33–36,45–50] Taking dense thin films of $SrTi_{1-x}Fe_xO_{3-\delta}$ (STF) as a model system to represent a mixed ionic electronic conducting (MIEC) perovskite oxide (ABO_3, where A and B denotes two different cations) electrode, we analyzed the surface composition and reactivity toward oxygen activation according to the temperature and the amount of thin-film misfit strain, finding that the amount of Sr-excess at the surface of STF epitaxial thin films could be controlled by manipulating the lattice strain.[36] The tensile strain in the in-plane direction considerably inhibits Sr enrichment and enhances the surface O_2 exchange rate. Subsequent DFT calculations revealed that relatively large Sr atoms in a STF lattice are subjected to compressive stress, and this local instability of Sr atoms drives the surface segregation. Thus, we suggested that adding an isovalent dopant larger than Ti to a B-site of perovskite would stabilize the Sr atom in the STF lattice with an extended Sr–O bond length and hence suppress the surface Sr-excess. However, experiments to verify this hypothesis have not been conducted thus far.

Department of Materials Science and Engineering, Korea Advanced Institute of Science and Technology (KAIST), Daejeon 34141, Republic of Korea. E-mail: wcjung@kaist.ac.kr

† Electronic supplementary information (ESI) available. See DOI: 10.1039/d0ta02870c

‡ Current address: Department of Mechanical Engineering, Massachusetts Institute of Technology, 77 Massachusetts Avenue, Cambridge MA 02139, USA.

This journal is © The Royal Society of Chemistry 2020

J. Mater. Chem. A, 2020, **8**, 13763–13769 | **13763**

To this end, here we choose Zr as an isovalent dopant to replace the Ti atom and thereby to stabilize Sr, after which we monitor the composition, morphology and reaction kinetics of the surface of the $SrTi_{0.5}Fe_{0.5}O_{3-\delta}$ film according to the presence or absence of Zr. Thin films of STF and 2 at% Zr-doped STF are prepared *via* pulsed laser deposition (PLD), and the values of the effective surface oxygen exchange coefficient (k_S) are obtained *via* electrical conductivity relaxation (ECR) tests at a temperature of 650 °C for 30 h. The physical and chemical attributes of each film sample are characterized by a range of analysis tools, in this case high-resolution X-ray diffraction (HR-XRD), X-ray fluorescence (XRF), X-ray photoelectron spectroscopy (XPS), and scanning transmission electron microscopy (STEM) with energy dispersive X-ray spectroscopy (EDS). Significantly, we succeed in confirming that the Zr dopant effectively suppresses the concentration of Sr on the surface and maintains excellent oxygen exchange reactivity levels without significant deterioration. The Zr-doped STF film shows a faster oxygen exchange rate by nearly one order of magnitude compared to undoped STF at 650 °C after 30 h. Furthermore, the nanoscale Sr-rich clusters frequently observed on the pristine STF surface upon annealing almost disappear after doping Zr, indicating that the less decreased surface reactivity is related to the formation of Sr-excess secondary phases on the surface, which the Zr dopant can inhibit. Convincingly, these observations indicate that the isovalent doping strategy can effectively improve the surface chemical stability of Sr-based perovskite oxides and provide a new perspective for achieving high-performance SOFC O$_2$-electrodes.

Experimental

Sample preparation

$SrTi_{0.5}Fe_{0.5}O_{3-\delta}$ (STF), 2 at% Zr-doped STF samples were prepared by a conventional solid-state reaction starting with $SrCO_3$ (Sigma Aldrich, ≥ 99.9%), TiO_2 (Alfa Aesar, 99.9%), Fe_2O_3 (Alfa Aesar, 99.945%), and ZrO_2 (Sigma Aldrich, 99.99% purity excluding ~2% HfO_2) powders. The powders were mixed to obtain the desired stoichiometric and ratio and were then ball-milled for 24 h with high-purity ethanol (Merck, 99.9%) before they were allowed to dry. The well-mixed powders were then calcined in air at 1250 °C for 8 h with heating and cooling rates of 4 °C min^{-1}. Pellet-type targets for pulsed laser deposition (PLD) were prepared by uniaxial pressing followed by cold isostatic pressing at 200 MPa. The compacted green bodies were sintered at 1425 °C for 8 h with heating and cooling rates of 4 °C min^{-1}. STF and Zr-doped STF films were deposited onto single-crystal Al_2O_3 (0001) substrates (10 mm × 10 mm × 0.65 mm, MTI Corporation) by the PLD technique from each target. The PLD system (VTS Corporation) was operated with a KrF excimer laser emitting at 248 nm (Coherent COMPex Pro 205) with energy of 280 mJ per pulse and a repetition rate of 10 Hz.[45–50] The substrates were heated to a heater setting temperature of 700 °C, which corresponds to approximately 560 °C as the actual temperature of the substrate surface, during the deposition step, while the oxygen pressure was maintained at 10 mTorr after pumping the background

pressure to 10^{-5} torr. After deposition and prior to cooling, the oxygen pressure in the chamber was increased to approximately 1 torr for 20 min to allow more complete oxidation of the films. The resulting films had a typical thickness of approximately 250 nm.

Physical and chemical characterization

High-resolution X-ray diffraction (HR-XRD, SmartLab, Rigaku) measurements were taken to assess the crystallinity of powder and the type of film of the STF and Zr-doped STF samples. The instrument was operated at 40 kV and 300 mA in range of 20° to 60° (θ–2θ scan) with a symmetric Johansson Ge (111) curved crystal using Cu Kα radiation ($\lambda = 1.541$ Å). Lattice parameters were extracted using the full pattern of the XRD results. An X-ray fluorescence (XRF, ZSX Primus II, Rigaku) spectrometer using the emission of secondary (or fluorescent) X-rays with an accelerating voltage of 60 kV and current of 100 mA was used for a quantitative compositional analysis of the synthesized STF and Zr-doped STF powders. Scanning electron microscopy (SEM, S-4800, Hitachi) was used to observe the thickness and morphological changes of the STF and Zr-doped STF thin films. To conduct secondary electrons, the films were coated *via* the osmium (Os) sputtering technique for 1 min under a vacuum. Cross-sectional scanning transmission electron microscopy (STEM, Titan cubed G2 60-300, FEI Co.) combined with energy dispersive X-ray spectroscopy (EDS) scans were carried out to identify the segregated clusters on the surfaces of the STF thin film sample after focused ion beam (FIB, Quanta 3D FEG, FEI company) milling at an acceleration voltage of 300 kV. X-ray photoelectron spectroscopy (XPS, K-alpha, Thermo VG Scientific) was conducted under an ultrahigh vacuum using monochromated Al Kα ($h\nu = 1486.6$ eV) radiation for a surface chemical composition of the polycrystalline STF and Zr-doped STF thin films. All of the XPS spectra were calibrated to the C–C peak (284.8 eV) in the C 1s spectrum based on the Shirley background.

Electrical conductivity relaxation (ECR) measurements

To take conductivity measurements of the STF and Zr-doped STF films, two platinum electrodes were applied to each of the films with a thickness of 200 nm and a 2 mm distance by DC magnetron sputtering (with DC power of 10 W, a working pressure of 10 mTorr under a flow rate of 30 sccm Ar, and a deposition rate of 60 nm min^{-1}) using a metal shadow mask. Before the measurements, residual segregated Sr which formed during the PLD procedure was removed by 100 mM of an HCl solution for 15 seconds.[29] A tube furnace with a K-type thermocouple was used for the measurement at 650 °C under various ratio between the O$_2$ and Ar gases (pO$_2$ (oxygen partial pressure) between 0.21 and 1 atm) with a total flow rate of 195 sccm controlled by a mass flow controller. The samples were initially kept at equilibrium and the pO$_2$ was abruptly changed with a four-way valve at a constant temperature. The in-plane conductivity, which reflects the oxygen content in the samples, was measured every 0.1 seconds until the sample adapted to the new equilibrium under applied DC current across the length of the specimen, with the voltage measured

13764 | *J. Mater. Chem. A*, 2020, **8**, 13763–13769

This journal is © The Royal Society of Chemistry 2020

via chronopotentiometry (CP, VSP-300, Biologic). Both the oxidation and reduction directions of the measurement were utilized in each condition so as to justify the assumption of a first-order surface oxygen exchange reaction.[33,36,51] The normalized conductivity as a function of time was fitted to a solution of the first-order surface oxygen exchange reaction equation as shown in Fig. S1.†

Results and discussion

The crystal structure of the powder and film-type STF and Zr-doped STF samples was characterized initially by means of HR-XRD. Fig. 1a shows XRD patterns of the STF and Zr-doped STF powders with Si reference powders. Both samples exhibit a cubic structure (space group: $Pm\bar{3}m$), but the average lattice parameter of the Zr-doped STF (3.8950 Å) is larger than that of STF (3.8907 Å), indicating that Zr doping extends the bond length between Sr and O, as shown in Fig. 1b.[36] To further confirm the effect of Zr doping level to stretch the Sr–O bond length, we also synthesized STF powders while varying the Zr concentration to 0.5, 1 and 2 at% and carried out an XRD analysis of each case. The results indicated that the average Sr–O bond length gradually increased according to the Zr doping concentration (Fig. S2 and Table S1†). Similarly, the Zr doping effect was found to show the same tendency in the as-grown STF film on the single-crystal c-Al$_2$O$_3$ (0001) substrate (Fig. 1c and d). The composition of the Zr-doped STF was also analyzed by XRF spectroscopy, showing good agreement in terms of the chemical formula of the perovskite oxide and the Zr doping (Table 1). A

trace amount of Hf was detected because it is the main contaminant contained in a typical Zr precursor.

To investigate the electrode activity toward the oxygen exchange of the samples, ECR measurements of the STF and Zr-doped STF were carried out at a temperature of 650 °C in an oxidizing atmosphere. Here, we fabricated STF and Zr-doped STF polycrystalline thin films by PLD on single-crystal c-Al$_2$O$_3$ (0001) substrates and deposited Pt thin-film electrodes onto them to measure the electrical conductance of each sample. It is important to note that the use of very thin and dense samples with nanoscale flatness is beneficial for an accurate measurement of the surface reaction rate. Because the thickness of both the undoped and doped STF films is below the critical thickness,[51] the conductivity relaxation profile reflects the kinetics of the surface oxygen exchange reaction rather than the bulk diffusion of oxygen. Therefore, the surface oxygen exchange coefficient (k_S) can be calculated using the following eqn (1),

$$\frac{\sigma(t) - \sigma(0)}{\sigma(\infty) - \sigma(0)} = 1 - \exp\left(-\frac{k_S}{a}t\right), \tag{1}$$

Table 1 Atomic ratio of each elements in SrTi$_{0.5}$Fe$_{0.5}$O$_{3-\delta}$ (STF) with Zr doping by X-ray fluorescence (XRF) analysis

At%	Sr	Ti	Fe	Hf	Zr
STF	50.3	24.9	24.8		
Zr doping	50.4	24.0	24.7	0.1	0.8

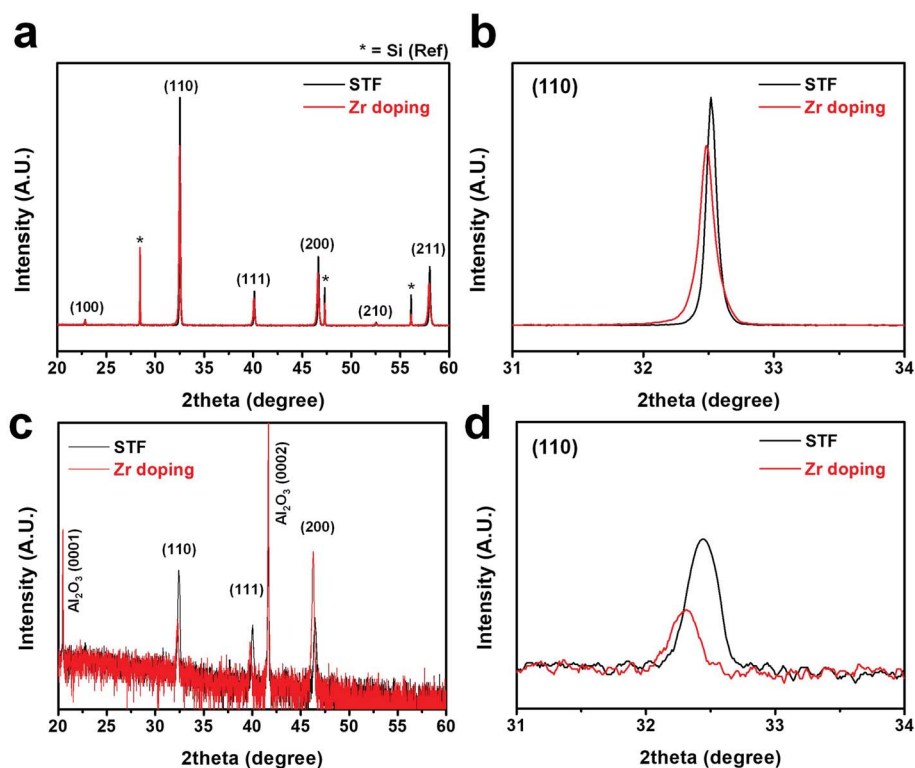**Fig. 1** (a) High-resolution X-ray diffraction (HR-XRD) result of SrTi$_{0.5}$Fe$_{0.5}$O$_{3-\delta}$ (STF) powder with Zr doping and (b) the detail pattern in (110) plane. (c) HR-XRD results of STF thin film with Zr doping on single-crystal c-Al$_2$O$_3$ (0001) and (d) the detail pattern in (110) plane.
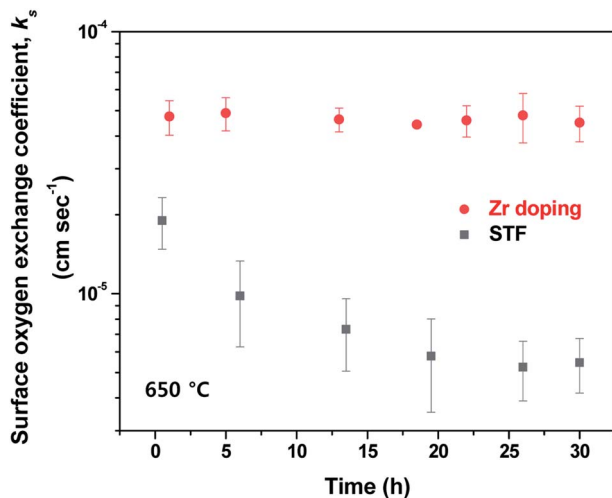
Fig. 2   Surface oxygen exchange kinetics of SrTi$_{0.5}$Fe$_{0.5}$O$_{3-\delta}$ (STF) thin film with Zr doping from electrical conductivity relaxation (ECR) measurements over time at 650 °C in air.

where $\sigma(t)$ and a represent the electrical conductivity at time t and the thickness of the STF film, respectively.[33,36,51] Fig. 2 shows the time-dependent change of k_S value for the STF films with/without Zr as a dopant obtained from the ECR measurements at 650 °C. It can be seen that the Zr dopant greatly improves the k_S value of STF. At the beginning of the measurement after the first equilibrium, k_S of the pristine STF is 2.24×10^{-5} cm s^{-1}, whereas the doped case shows a slightly higher k_S value of 5.88×10^{-5} cm s^{-1}. These observations indicate that the deterioration of undoped STF electrode activity has already proceeded at the initial measurement after the first equilibrium state. Furthermore, as time elapses, the difference between the two samples becomes even greater. For

example, after the measurement for 30 h, k_S of the STF film is reduced greatly as 72% compared to the initial level, while the Zr doping holds the k_S value mostly steady, without any deterioration. As a result, the presence of Zr dopants maintains the k_S value of the STF film for 30 h. It is therefore obvious that the addition of Zr into the Ti site secures the oxygen exchange rate of the STF surface and inhibits its evolution over time. To the best of our knowledge, these observations are the very first evidence confirming that the iso-valent doping strategy actually works for perovskite-based O$_2$-electrodes for SOFCs, as predicted in our previous report.[9,34,36]

Next, in order to confirm whether the degradation of the reaction rate observed in this study is related to the surface Sr-excess, we investigated the surface morphology and chemical composition of the samples after the ECR measurements via SEM, TEM and XPS analyses. Fig. 3 shows SEM top-view images of STF and Zr-doped STF thin-film samples before/after the ECR measurements at 650 °C for 30 h. Several clusters 80–500 nm in size, presumably formed by Sr enrichment and phase separation, were observed on the surface of the pristine STF thin film. The Zr-doped sample, in contrast, maintains a fairly flat surface without noticeable clusters after the heat treatment. A slight change in the surface roughness was observed, but this is closer to thermally driven surface restructuring as opposed to any secondary formation.

Cross-sectional STEM and EDS analyses further demonstrate that the observed clusters stem from Sr segregation. Fig. 4 shows the STEM-EDS elemental mapping of the STF and Zr-doped STF thin films after the ECR measurement at 650 °C for 30 h. In the STF case, it is clearly shown that the cluster formed mainly consists of Sr and O as SrO$_x$, representing significant Sr enrichment. However, the EDS mapping images revealed that Ti and Fe were homogeneously distributed in the STF thin films. In contrast, Ti, Fe, Zr, as well as Sr elements were
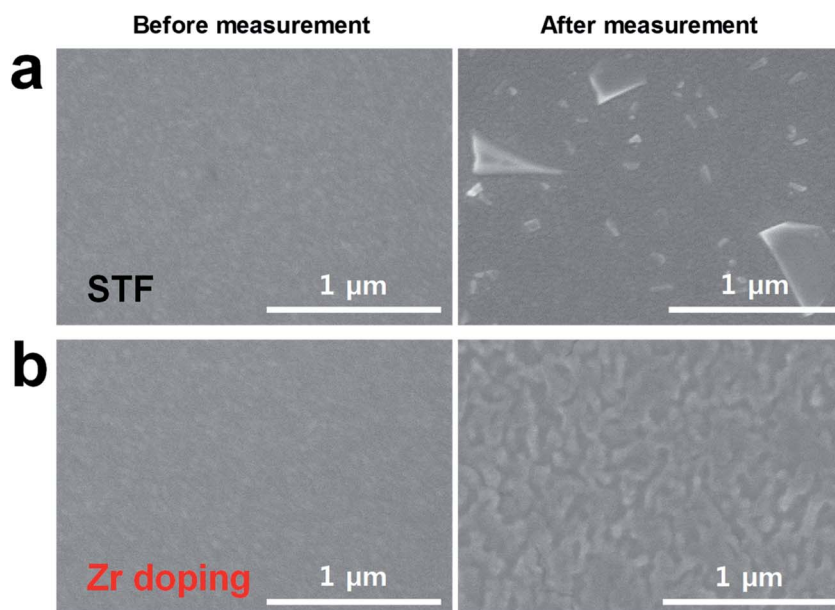

Fig. 3   (a) Surface morphological changes of SrTi$_{0.5}$Fe$_{0.5}$O$_{3-\delta}$ (STF) thin films (b) with Zr doping before/after electrical conductivity relaxation (ECR) measurements by means of scanning electron microscopy (SEM).
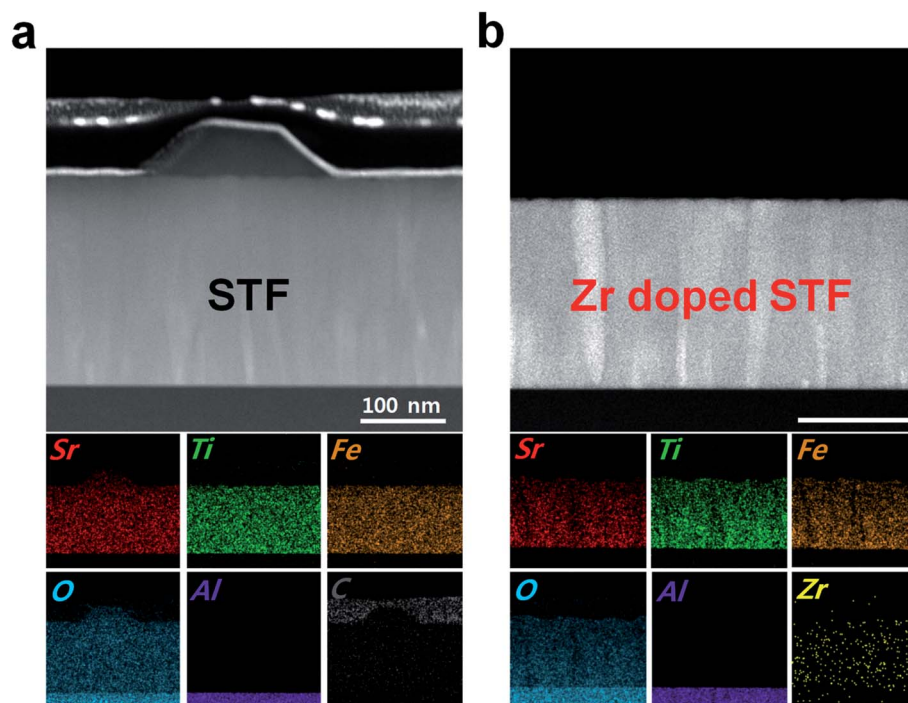
Fig. 4 (a) Cross-sectional high-angle annular dark-field (HAADF) and energy dispersive X-ray spectroscopy (EDS) images for the $SrTi_{0.5}Fe_{0.5}O_{3-\delta}$ (STF) and (b) Zr-doped STF films after ECR measurement by means of transmission electron microscopy (TEM).

finely distributed in the Zr-doped STF; thus, there is no Sr-excess or accumulation on the surface of the doped STF. To assess the degree of heterogeneity at higher spatial resolutions, a STEM-EDS line scanning analysis was also attempted. EDS line profiles at a total of five points spaced 40 nm apart in the horizontal direction from the Sr-rich isolate are shown in Fig. 5. The graph below the STEM image shows the cation fraction (Sr : Ti : Fe) from the EDS line scanning analysis as a function of the depth of the STF film (in the vertical direction of each point). For all points, the cation stoichiometry is consistent with the relative composition ratio of STF (Sr : Ti : Fe = 0.5 : 0.25 : 0.25)

for the interior of the STF film. With the ideal stoichiometry of Sr (0.5) as an index, it could be observed that a noticeable change in the distribution of Sr on the STF surface is in a depth of approximately 20 nm from the surface. The SrO_x cluster, which formed on the surface of the STF electrode after the ECR measurements is composed mostly of Sr cations, as shown in Fig. 5e. Nontrivial levels of Sr deficiency were also observed on surfaces near Sr-rich clusters that appeared to be flat and clean. As shown in Fig. 5a–e, the surface at a depth of 30 to 50 nm contains less Sr than the stoichiometric composition, even in the horizontal region 160 nm away from the edge of the Sr-rich
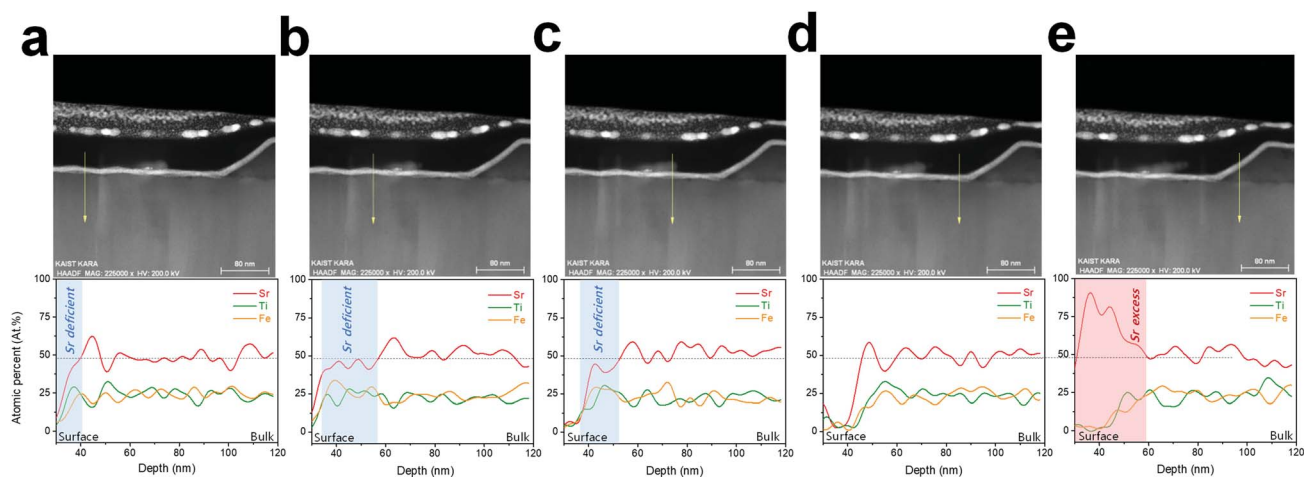

Fig. 5 Cross-sectional high-angle annular dark-field (HAADF) images and EDS line scanning analysis for the $SrTi_{0.5}Fe_{0.5}O_{3-\delta}$ (STF) after ECR measurement at 40 nm intervals from the edge of the Sr-rich phase by means of transmission electron microscopy (TEM): (a) 160 nm, (b) 120 nm (c) 80 nm, (d) 40 nm, and (e) 0 nm from the edge of the Sr-rich phase.

Table 2 Surface chemical composition of $SrTi_{0.5}Fe_{0.5}O_{3-\delta}$ (STF) thin films with Zr doping after ECR measurements by X-ray photoelectron spectroscopy (XPS) analysis

At%	Sr	Ti	Fe	Zr	Sr/B-site
STF	61.40	29.55	9.05	0.00	1.59
Zr doping	50.11	28.36	20.16	1.36	1.00

clusters. These findings indicate that the diffusion of Sr cations led to the formation of a Sr-enriched phase during the ECR measurements. Recently, Lee *et al.* reported a similar result demonstrating that SrO_x precipitates formed from a depth of approximately 25 nm from the $La_{0.6}Sr_{0.4}Co_{0.2}Fe_{0.8}O_{3-\delta}$ surface through the surface diffusion of Sr ions, resulting in Sr deficiency of the exposed clean surface of the $La_{0.6}Sr_{0.4}Co_{0.2}Fe_{0.8}O_{3-\delta}$ sample.[52] They concluded that the inherently low reactivity of the Sr-deficient region around the SrO_x clusters may be a major cause of the degradation of the perovskite electrode by Sr segregation.

The surface chemical composition of each film was also analyzed *via* XPS analysis (Fig. S3†) while focusing on the effects of Zr doping in STF after the ECR measurements. Table 2 presents the XPS quantitative analysis results. After the measurements at 30 h, the undoped film shows that the surface Sr concentration is greatly deviated from the bulk stoichiometry, indicating that excess Sr exists on the surface, whereas the Zr-doped STF has a negligible degree of Sr enrichment on the surface. As a result, the Sr-excess was suppressed by Zr doping in the B-sites of STF perovskite oxides, closely related to the stability improvement and the improved electrode activity.

Based on the discussion thus far, it is apparent that Zr doping in STF considerably prevents surface Sr enrichment and thereby facilitates the surface oxygen exchange rate. It is believed that a longer Sr–O bond length and stronger Sr–O bond realized by replacing Ti with a larger cation, Zr, can stabilize the Sr atoms in the STF crystal lattice. Previously, we also observed significant degradation of STF thin film electrodes by a SrO_x-related species on the STF surfaces, which served as a passivation barrier for oxygen exchange.[31,34] Considering these results, it is clear that Sr–O bonds strengthened by isovalent doping mitigate the formation of insulating SrO_x on the surface and thereby passivation or deactivation of the STF surfaces, eventually activating the surface oxygen exchange. It is noteworthy that, as observed in the STEM-EDS line scan, there are Sr-deficient regions around the SrO_x clusters which appear clean but should not be ruled out as a possible cause of surface reactivity degradation.[52] Thus, the substitution of isovalent B-site cations with larger ionic radii could be a practical means of controlling the stability effectively for the suppression of the surface Sr enrichment and to improve the long-term stability of Sr-based perovskite-type O_2-electrodes. We think the isovalent B-site doping strategy readily applicable to actual SOC O_2-electrodes.

Recently, Yildiz and co-workers reported that a surface modification with less reducible cations can lead to lower the concentration of surface oxygen vacancies ($V_O^{\cdot\cdot}$) that are positively charged, and reduce the electrostatic attraction of negatively charged Sr dopants (Sr'_{La}) towards a $La_{0.8}Sr_{0.2}CoO_3$ (LSC) surface.[29] The essence of their study was that it presented a method by which to control the electrostatic interaction between $V_O^{\cdot\cdot}$ and Sr'_{La} to prevent surface Sr segregation. There is similarity between this study and the earlier work by Yildiz and co-workers in that an additional cation other than the main constituent of the perovskite electrode stabilizes the surface of SOFC O_2-electrodes. However, our study focuses on the elastic driving force for Sr segregation. In LSC, a Sr cation is an aliovalent dopant with an effectively negative charge, whereas in STF, it is a neutral constituent. Because strain may have a slight effect on the charge states of the constituent ions, it does not significantly alter the electrostatic interactions for either perovskite, but instead directly changes the Sr segregation due to the elastic interactions. Therefore, this study enables us effectively to identify the elastic effect on the Sr segregation using an isovalent dopant: the extension of the Sr–O bond length in STF.

Conclusion

In summary, we investigated the effects of isovalent (Zr replacing the Ti site) doping on the oxygen exchange kinetics, surface morphology and chemical composition of thin-film-type $SrTi_{0.5}Fe_{0.5}O_{3-\delta}$ (STF) as a typical model perovskite O_2-electrode. Zr doping in STF considerably inhibits Sr enrichment and facilitates the surface oxygen exchange rate by a factor of 8.8 compared to a pristine STF O_2-electrode at 650 °C after 30 h. The segregated particles formed by phase separation on the surface of the STF O_2-electrode after electrode reactivity tests were found to be SrO_x species. The findings here confirm that isovalent doping in B-sites is a useful method for preventing surface Sr-excess. Moreover, this approach can easily be applied to ensure the surface stability of Sr-containing perovskite oxides for SOFC O_2-electrodes under actual operating conditions.

Conflicts of interest

There are no conflicts to declare.

Acknowledgements

References

1 N. Q. Minh, *J. Am. Ceram. Soc.*, 1993, **76**(3), 563–588.
2 S. M. Haile, *Acta Mater.*, 2003, **51**, 5981–6000.
3 S. C. Singhal, *Solid State Ionics*, 2002, **152–153**, 405–410.

4 J. H. Kim, J. K. Kim, H. G. Seo, D.-K. Lim, S. J. Jeong, J. Seo, J. Kim and W. Jung, *Adv. Funct. Mater.*, 2020, 2001326.

5 H. G. Seo, S. Ji, J. Seo, S. Kim, B. Koo, Y. Choi, H. Kim, J. H. Kim, T.-S. Kim and W. Jung, *J. Alloys Compd.*, 2020, **835**, 155347.

6 Y. Choi, S. K. Cha, H. Ha, S. Lee, H. K. Seo, J. Y. Lee, H. Y. Kim, S. O. Kim and W. Jung, *Nat. Nanotechnol.*, 2019, **14**, 245–251.

7 Z. Shao and S. M. Haile, *Nature*, 2004, **431**, 170–173.

8 H. Kim, H. G. Seo, Y. Choi, D.-K. Lim and W. Jung, *J. Mater. Chem. A*, 2020, DOI: 10.1039/D0TA02439B.

9 B. Koo, K. Kim, J. K. Kim, H. Kwon, J. W. Han and W. Jung, *Joule*, 2018, **2**, 1476–1499.

10 H. G. Seo, Y. Choi, B. Koo, A. Jang and W. Jung, *J. Mater. Chem. A*, 2016, **4**, 9394–9402.

11 J. Druce, H. Téllez, M. Burriel, M. D. Sharp, L. J. Fawcett, S. N. Cook, D. S. McPhail, T. Ishihara, H. H. Brongersma and J. A. Kilner, *Energy Environ. Sci.*, 2014, **7**, 3593–3599.

12 W. Jung and H. L. Tuller, *J. Electrochem. Soc.*, 2008, **155**, B1194–B1201.

13 W. Jung and H. L. Tuller, *Solid State Ionics*, 2009, **180**, 843–847.

14 L. Wang, R. Merkle, Y. A. Mastrikov, E. A. Kotomin and J. Maier, *J. Mater. Res.*, 2012, **27**, 2000–2008.

15 Y. M. Choi, M. C. Lin and M. Liu, *Angew. Chem., Int. Ed.*, 2007, **119**, 7352–7357.

16 S. Choi, S. Yoo, J. Kim, S. Park, A. Jun, S. Sengodan, J. Kim, J. Shin, H. Y. Jeong, Y. M. Choi, G. Kim and M. Liu, *Sci. Rep.*, 2013, **3**, 2426.

17 V. Metlenko, W. Jung, S. R. Bishop, H. L. Tuller and R. A. De Souza, *Phys. Chem. Chem. Phys.*, 2016, **18**, 29495–29505.

18 M. Pavone, A. M. Ritzmann and E. A. Carter, *Energy Environ. Sci.*, 2011, **4**, 4933–4937.

19 M. Choi, I. A. M. Ibrahim, K. Kim, J. Y. Koo, S. J. Kim, J.-W. Son, J. W. Han and W. Lee, *ACS Appl. Mater. Interfaces*, 2020, **12**(19), 21494–21504.

20 S.-L. Zhang, H. Wang, M. Y. Lu, A.-P. Zhang, L. V. Mogni, Q. Liu, C.-X. Li, C.-J. Li and S. A. Barnett, *Energy Environ. Sci.*, 2018, **11**, 1870–1879.

21 M. Y. Lu, J. G. Railsback, H. Wang, Q. Liu, Y. A. Chart, S.-L. Zhang and S. A. Barnett, *J. Mater. Chem. A*, 2019, **7**, 13531–13539.

22 S.-L. Zhang, D. Cox, H. Yang, B.-K. Park, C.-X. Li, C.-J. Li and S. A. Barnett, *J. Mater. Chem. A*, 2019, **7**, 21447–21458.

23 W. Jung and H. L. Tuller, *Adv. Energy Mater.*, 2011, **1**, 1184–1191.

24 E. J. Crumlin, E. Mutoro, W. T. Hong, M. D. Biegalski, H. M. Christen, Z. Liu, H. Bluhm and Y. Shao-Horn, *J. Phys. Chem. C*, 2013, **117**, 16087–16094.

25 H. Jalili, J. W. Han, Y. Kuru, Z. Cai and B. Yildiz, *J. Phys. Chem. Lett.*, 2011, **2**, 801–807.

26 Z. Feng, Y. Yacoby, M. J. Gadre, Y.-L. Lee, W. T. Hong, H. Zhou, M. D. Biegalski, H. M. Christen, S. B. Adler, D. Morgan and Y. Shao-Horn, *J. Phys. Chem. Lett.*, 2014, **5**, 1027–1034.

27 M. Kubicek, A. Limbeck, T. Frömling, H. Hutter and J. Fleig, *J. Electrochem. Soc.*, 2011, **158**, B727–B734.

28 Z. Cai, M. Kubicek, J. Fleig and B. Yildiz, *Chem. Mater.*, 2012, **24**, 1116–1127.

29 N. Tsvetkov, Q. Lu, L. Sun, E. J. Crumlin and B. Yildiz, *Nat. Mater.*, 2016, **15**, 1010–1016.

30 W. Lee, J. W. Han, Y. Chen, Z. Cai and B. Yildiz, *J. Am. Chem. Soc.*, 2013, **135**, 7909–7925.

31 Y. Chen, W. Jung, Z. Cai, J. J. Kim, H. L. Tuller and B. Yildiz, *Energy Environ. Sci.*, 2012, **5**, 7979–7988.

32 G. M. Rupp, A. K. Opitz, A. Nenning, A. Limbeck and J. Fleig, *Nat. Mater.*, 2017, **16**, 640–646.

33 Y. Kim, S. J. Jeong, B. Koo, S. Lee, N. W. Kwak and W. Jung, *J. Mater. Chem. A*, 2018, **6**, 13082–13089.

34 W. Jung and H. L. Tuller, *Energy Environ. Sci.*, 2012, **5**, 5370–5378.

35 T.-S. Oh, Y. S. Tokpanov, Y. Hao, W. Jung and S. M. Haile, *J. Appl. Phys.*, 2012, **112**, 103535.

36 B. Koo, H. Kwon, Y. Kim, H. G. Seo, J. W. Han and W. Jung, *Energy Environ. Sci.*, 2018, **11**, 71–77.

37 A. Lussier, J. Dvorak, S. Stadler, J. Holroyd, M. Liberati, E. Arenholz, S. B. Ogale, T. Wu, T. Venkatesan and Y. U. Idzerda, *Thin Solid Films*, 2008, **516**, 880–884.

38 K. K. Hansen and K. Vels Hansen, *Solid State Ionics*, 2007, **178**, 1379–1384.

39 Y. Zhu, Z. -G. Chen, W. Zhou, S. Jiang, J. Zou and Z. Shao, *ChemSusChem*, 2013, **6**, 2249–2254.

40 Y. Gong, D. Palacio, X. Song, R. L. Patel, X. Liang, X. Zhao, J. B. Goodenough and K. Huang, *Nano Lett.*, 2013, **13**(9), 4340–4345.

41 W. Lee and B. Yildiz, *ECS Trans.*, 2013, **57**(1), 2115–2123.

42 X. Zhu, D. Ding, Y. Li, Z. Lü, W. Su and L. Zhen, *Int. J. Hydrogen Energy*, 2013, **38**, 5375–5382.

43 D. Lee, Y.-L. Lee, A. Grimaud, W. T. Hong, M. D. Biegalski, D. Morgan and Y. Shao-Horn, *J. Phys. Chem. C*, 2014, **118**(26), 14326–14334.

44 J. Y. Koo, H. Kwon, M. Ahn, M. Choi, J.-W. Son, J. W. Han and W. Lee, *ACS Appl. Mater. Interfaces*, 2018, **10**(9), 8057–8065.

45 N. W. Kwak, S. J. Jeong, H. G. Seo, S. Lee, Y. Kim, J. K. Kim, P. Byeon, S.-Y. Chung and W. Jung, *Nat. Commun.*, 2018, **9**, 4829.

46 Y.-R. Jo, B. Koo, M.-J. Seo, J. K. Kim, S. Lee, K. Kim, J. W. Han, W. Jung and B.-J. Kim, *J. Am. Chem. Soc.*, 2019, **141**, 6690–6697.

47 J. Seo, N. Tsvetkov, S. J. Jeong, Y. Yoo, S. Ji, J. H. Kim, J. K. Kang and W. Jung, *ACS Appl. Mater. Interfaces*, 2020, **12**, 4405–4413.

48 J. K. Kim, Y.-R. Jo, S. Kim, B. Koo, J. H. Kim, B.-J. Kim and W. Jung, *ACS Appl. Mater. Interfaces*, 2020, **12**, 24039–24047.

49 K. Kim, B. Koo, Y.-R. Jo, S. Lee, J. K. Kim, B.-J. Kim, W. Jung and J. W. Han, *Energy Environ. Sci.*, 2020, DOI: 10.1039/D0EE01308K.

50 S. J. Jeong, N. W. Kwak, P. Byeon, S.-Y. Chung and W. Jung, *ACS Appl. Mater. Interfaces*, 2018, **10**, 6269–6275.

51 R. Merkel and J. Maier, *Angew. Chem., Int. Ed.*, 2008, **47**, 3874–3894.

52 D. Kim, J. W. Park, B.-H. Yun, J. H. Park and K. T. Lee, *ACS Appl. Mater. Interfaces*, 2019, **11**, 31786–31792.

This journal is © The Royal Society of Chemistry 2020

J. Mater. Chem. A, 2020, **8**, 13763–13769 | **13769**